Experimental study of swelling of organic rich shale in methane

Tianyu Chen, Xia-Ting Feng, Zhejun Pan

PII: S0166-5162(15)30034-3
DOI: doi: 10.1016/j.coal.2015.08.001
Reference: COGEL 2507

To appear in: *International Journal of Coal Geology*

Received date: 28 January 2015
Revised date: 31 July 2015
Accepted date: 3 August 2015

Please cite this article as: Chen, Tianyu, Feng, Xia-Ting, Pan, Zhejun, Experimental study of swelling of organic rich shale in methane, *International Journal of Coal Geology* (2015), doi: 10.1016/j.coal.2015.08.001

Experimental study of swelling of organic rich shale in methane

Tianyu Chen[a], Xia-Ting Feng[a,b,*], and Zhejun Pan[c]

[a]*Key Laboratory of Ministry of Education on Safe Mining of Deep Metal Mines, Northeastern University, Shenyang 110004, China*

[b]*State Key Laboratory of Geomechanics and Geotechnical Engineering, Institute of Rock and Soil Mechanics, Chinese Academy of Sciences, Wuhan 430071, China*

[c]*CSIRO Energy Flagship, Private Bag 10, Clayton South VIC 3169, Australia*

Abstract

Gas is stored in shale mainly in free and adsorbed phases. Since a significant amount of gas in the shale is adsorbed to the organic matter and/or clay minerals, it is possible that gas adsorption will induce shale swelling, which may then has an impact on the gas flow behavior in the shale thus its gas production. In this work, strain behavior was studied in two gases, helium and methane, at different pore pressures under constant hydrostatic pressure at 20 MPa on two shale samples. The results show that porosity and volumetric strain are functions of gas pressure and the strain is larger in methane than helium demonstrating gas adsorption induced swelling for the shale samples. The calculated methane adsorption induced swelling strain is at a magnitude of 0.1% volumetrically with pressure at 10 MPa for the shale samples studied. The adsorption induced shale swelling strain shows a Langmuir-like relationship with pressure and is proportional to the amount of methane adsorbed. The results also show slight anisotropic strain behavior between the two directions of parallel and perpendicular to the bedding and strain hysteresis with methane in and out of the shale. The gas adsorption induced swelling may influence gas flow in gas shale, thus more research in this topic is warranted.

Keywords: Gas shale, shale gas, adsorption, strain, anisotropy, methane

* Corresponding author. Tel.: +86 27 8719 8913; *E-mail address*: xtfeng@whrsm.ac.cn, xia.ting.feng@gmail.com

1. Introduction

With the successful exploration and development of shale gas reservoirs in the USA, shale gas has received increasing interests from many other countries as an alternative hydrocarbon resource (Hartwig and Schulz, 2010; Soroush et al., 2010; Tan et al., 2014). Despite the success of shale gas production in the North America, shale gas is difficult to produce due to its low reservoir permeability and gas storage behavior. Gas shale is rich in organic carbon and clay minerals, resulting in significant amount of methane being adsorbed, along with compressed free gas in other pores (e.g., Labani et al., 2013; Yu and Sepehrnoori, 2014). Adsorption is one of the key gas storage mechanisms as 20% to 85% of the gas in place is adsorbed in shale (Hill and Nelson, 2000) and it has a significant impact on gas production behavior (Pan and Connell, 2015).

Shale is composed with complex mineral pore and fracture network which is the main site for gas storage and pathway for gas transport. At reservoir conditions, as gas is produced and gas pressure decreases, the shale may experience strain change as a poroelastic material due to the effective stress change. This would affect the pore structures thus the gas flow behavior in the shale pore/fracture system. Moreover, since a significant amount of gas in the shale is adsorbed to the organic matter and/or clay minerals, it may also cause adsorption-induced strain change, as adsorption/desorption changes surface potential energy of the adsorbent leading to its swelling/shrinkage (Pan and Connell, 2007). The sorption-induced shale swelling/shrinkage will also lead to the change of pore structure at reservoir conditions, further impacting on the gas flow behavior in the shale.

Gas adsorption in shale has been studied extensively especially recently. However, all these adsorption measurements are mainly focused on the adsorption capacity of the gas shale and the various factors affecting adsorption (Chalmers et al., 2012; Chareonsuppanimit et al., 2012; Gasparik et al., 2014; Guo, 2013; Lu et al., 1995; Ross and Marc Bustin, 2009; Weniger et al., 2010; Zhang et al., 2012). Nevertheless, there has been no laboratory measurement of swelling on shale associated to gas adsorption (Heller and Zoback, 2014). Heller and Zoback (2014) used pure mineral particles of carbon, illite and kaolinite instead of natural shale samples to indirectly investigate the importance of swelling in gas shale, due to the long equilibration time and small swelling strain of adsorption-induced shale swelling. Other shale swelling measurement has been using water or its vapor (e.g., Yuan et al., 2014a). However water-shale interaction is different as clay minerals have strong interaction with water and the mechanism of water induced swelling is different to that of the gas adsorption induced shale swelling. Thus it is important to study the gas adsorption induced shale swelling, which could provide insight to the gas and shale interaction and gas transport in shales.

In this work, laboratory measurements of adsorption capacity and corresponding strains,

including axial strain and radial strain, on two gas shale samples were carried out under constant hydrostatic pressure. Helium was first used to study the strain behavior as helium is considered non–adsorbing to shale at reservoir temperature and methane was then used to study the adsorption and shale strain behavior. Then adsorption-induced swelling strain was analyzed based on the experimental strain data in helium and methane. Strain anisotropy and hysteresis were also investigated.

2. Experimental

2.1 Shale samples

Shale samples used in this study were recovered from the outcrop of the lower Cambrian Niutitang formation in Hunan province, Southern China. The lower Cambrian Niutitang formation is one of the main target formations for shale gas exploration in China (Tian et al., 2015). Sampling location at Taoyuan county is located in the northwest of Hunan province, which belongs to upper yangtze platform (Lin et al., 2014). The main geological structures and the sampling location are shown in Fig. 1. There are three main formations in the Lower Cambrian in the northwest of Hunan province, the Niutitang, Palang and Qingxudong formations from bottom to up. The hydrocarbon-producing organic rich shales are mainly developed in the Niutitang formation, which was deposited in deep-water shelf environment during Paleozoic Marine sedimentary (Wang et al., 2014; Zhang et al., 2014). Shales in Niutitang formation have good gas production potential because of its large distribution area, large thickness, high organic carbon contents and high thermal maturity, and it is considered as the key breakthrough area of shale gas exploration in Southern China (He et al., 2015; Lin et al., 2014; Nie et al., 2011). Northwestern areas of Hunan province have gone through repeated tectonic movements, where drape and fault structures have developed. The Lower Cambrian organic rich shale formations developed in the northwest of Hunan province are controlled by Huahuan-Cili large abyssal fault. Thickness of the organic rich shales gradually decreases from northwest to southeast of Hunan province, and the maximum thickness is about 200 meters (Xiao et al., 2012; Zhang et al., 2014). Shale gas reservoirs in northwestern areas of Hunan province have experienced large tectonic uplift and its geological conditions are similar to that of Eastern United States (Xiao et al., 2012).

The mineral compositions of the two samples were determined using X-ray diffraction (Table 1). Quartz, feldspar, and pyrite are the brittle mineral components, which combined about 68.08% of the total mineral content for Sample1 and 68.32% for Sample2. The average content of clay minerals is about 25.18% for Sample1 and 24.51% for Sample2. The dominant clay mineral type is illite, which has a high gas adsorption and storage capacity (Heller and Zoback, 2014; Lu et al., 1995). Clay minerals are often mixed with organic matter in gas shale. A high clay mineral content implies the shale contains a large number of

pores which provide space for gas to occur and migrate (Hou et al., 2014).

The total organic carbon (TOC) and vitrinite reflectance (R_o) results of the two samples are also summarized in Table 1. The organic matter in the samples is type II kerogen. The TOC of the shale is the most important factor that controls methane adsorption capacity (Hou et al., 2014) and methane adsorption capacity is positively correlated with TOC (Lu et al., 1995; Zhang et al., 2012). The organic matter contains the main adsorption sites in which nanometer-sized pores exist (Loucks et al., 2009). When the shale maturity is greater than 0.60% R_o, a large number of nanometer-sized pores can be observed in organic matter (Loucks et al., 2009). The average TOC of the two samples is about 6.96%, which suggests that the samples may have high adsorption capacity. Furthermore, the samples have high maturity at about 2.45 $R_{o,max}$% (Table 1), which also suggests that the shale may have high adsorption capacity. As gas shale with high maturity has pores with large specific surface areas, this makes the gas adsorption capacity correspondingly higher (Ross and Marc Bustin, 2009).

Samples were prepared to cylinders at diameter of 50 mm and length of 100 mm for adsorption and strain measurements. Considering that gas migrate mainly along the bedding direction, the samples were drilled parallel to the bedding. Using the samples drilled parallel to the bedding, gas can flow quickly into the microfractures and pores developed on the bedding plane and then migrate into the shale matrix, so that gas in the shale samples can reach saturation state faster. To avoid damaging the original pore structure of the shale, the core samples were dried in a vacuumed chamber at room temperature for a few days until its weight did not change. After drying, the weight of the two samples was 436.25 and 432.51 g.

2.2 Pore structure characterization

Fresh surfaces of the shale samples were polished by argon ion beam milling system at an accelerating voltage of 4 kV for six hours. Mineral grains, pores, and microfractures in the shale samples were observed by scanning electron microscope (Quanta 200F) under the condition of back scattering. Mineral compositions were determined using energy spectrum analysis.

Micropore surface area, volume, and size distribution in the shale samples were obtained by N_2 adsorption at 77K using NOVA1000e surface area and pore size analyzer. The off-cuts of the two samples were crushed into grains of about 1mm in size. The prepared graininess samples were dried in an oven at 105℃ for 10 h before the tests and then degassed in the pore size analyzer for another 10 h. The relative pressure was applied from 0.04 to 0.98 during the testing process. Surface area and pore size distribution were calculated using Brunauer–Emmett–Teller (BET) and Barrett-Joyner-Halenda (BJH) models.

2.3 Adsorption and strain experimental setup

Adsorption and swelling experiments were carried out using a coupled, multi-field testing apparatus as shown schematically in Fig. 2. The apparatus mainly consists of a triaxial cell, an axial loading system, a confining pressure control system, a gas injection system, a vacuum system, a temperature control system, and a data acquisition system. The triaxial cell is equipped with an auto-balance piston, which can provide a hydrostatic pressure environment for adsorption and swelling experiments. The confining pressure of the system can reach up to 100 MPa and the axial loading pressure can reach up to 380 MPa.

The sample is wrapped in a thermal-shrinkable sleeve and two axial linear variable differential transformers (LDVT) and one radial LVDT are used to measure the deformation of the sample. All LDVTs have a precision of 0.1 μm. Both axial LVDTs are fixed between the top and bottom platens, and the radial LVDT is fixed at the middle of the sample.

Gas is injected from the ISCO injection pump to both the top and bottom of the sample. The ISCO injection pump can accurately monitor and record the volume change, which is determined by measuring the change in displacement of a step motor to a precision of 4.825 nl. The temperature control system can provide a constant temperature environment for the sample and injected gas with a precision of ± 0.1 °C.

2.4 Adsorption and strain measurements and calculation

2.4.1 Gauge calibration

Before any measurement, a stainless steel sample was used to calibrate the void volume of the system and the error of LDVT gauges. The steel sample is 50 mm in diameter and 100 mm in length and it is the same size as the shale samples. A hydrostatic pressure is applied to the steel sample and the system was vacuumed. Helium was then charged to the ISCO injection pump, which was controlled at constant pressure model. After the helium reached equilibrium state in the pump, it was then injected to the system. The dead volume of the system can be calculated from the pump volume change. For each gas pressure stage, the injection pump was maintained at constant-pressure for 24 hours to determine whether a gas leak occurs at that pressure.

During the experiments, the sample was placed between the top and bottom platens. Two axial LVDTs were installed between the platens and they were on opposite sides of the sample. When gas was injected, it quickly flowed into the gap between the platens and sample, causing an instantaneous spring-back response of the axial LVDT. This part of the axial displacement does not correspond to the displacement of the shale sample and belongs to system error. Since the radial LVDT is fixed onto the outside of the thermal-shrinkable sleeve, the measured displacement contains the sleeve's deformation. Same to the axial LDVT response to gas injection, an instantaneous spring-back response of the radial LVDT

was also observed when gas was injected. Moreover, the deformation of the sleeve occurs during pressure change. Therefore, all LVDTs needed to be calibrated to obtain accurate displacement of the shale sample during gas injection. The stainless steel sample was used to calibrate these errors. The hydrostatic pressure was first applied to the steel calibration sample, and then different gas pressure was applied. The displacements from the axial and radial LDVTs on the steel calibration sample at different gas pressure were measured and used as calibration. For each gas pressure step, a constant pressure mode was maintained for 24 hours to detect the deformations.

2.4.2 Helium porosity

After installing the shale core sample in the apparatus, helium was injected into the shale sample through the injection pump at controlled pressure mode. When the volume in the pump became unchanged, the gas in the shale had reached equilibrium. The total void volume, which includes the void volume of the system and the pore volume, can be calculated by:

$$V_{total}^{i} = \frac{Z_i}{P_i} \times \sum_{j=1}^{i} \frac{P_j V_j}{Z_j} \tag{1}$$

Where P_i is the gas pressure at each injection step, V_{total}^{i} is the total void volume, V_i is the injected volume measured using the injection pump at pressure P_i, and Z_i is the compressibility factor of the injected gas at pressure P_i. The gas compressibility factor was calculated using the National Institute of Standards and Technology (NIST) WebBook (http://webbook.nist.gov/chemistry/fluid/).

The pore volume can be obtained by subtracting the system void volume from the total void volume:

$$V_{poro}^{i} = V_{total}^{i} - V_{void} \tag{2}$$

Where V_{poro}^{i} is the pore volume of the shale at pressure P_i, V_{void} is the system void volume. Porosity at each pressure step, ϕ^i, can be calculated by:

$$\phi^i = \frac{V_{poro}^{i}}{V_b} \tag{3}$$

Where V_b is the bulk volume of the shale sample.

2.4.3 Methane adsorption

Methane adsorption experiments were carried out using the same procedures as the helium porosity experiments. The difference is mainly in the calculation. The amount of excess adsorption is obtained by subtracting the amount of gas in all the void volume from the total injected amount:

$$n_{\text{ads}}^{Gibbs} = n_{total} - n_{void} - n_{poro} \tag{4}$$

Where n_{ads}^{Gibbs} is the Gibbs excess adsorption, n_{total} is the total amount of methane injected from the pump to the system, n_{void} is the amount of methane in the system void volume, n_{poro} is the amount of methane in the pores of the shale sample. The absolute adsorption amount can be converted from the Gibbs excess adsorption isotherm by using:

$$n_{\text{ads}}^{Abs} = n_{\text{ads}}^{Gibbs}\left(\frac{\rho_{ads}}{\rho_{ads} - \rho_{gas}}\right) \tag{5}$$

Where n_{ads}^{Abs} is the absolute adsorption amount, ρ_{gas} is the gas phase density, which is also calculated from the NIST Webbook, and ρ_{ads} is the adsorbed phase density, which is 0.421 g/ml as often used in methane adsorption in coals (Fitzgerald et al., 2005).

Desorption measurement was carried out after the methane adsorption reached at 10 MPa. During desorption, the pump pressure was controlled at a lower pressure than the gas pressure in the sample and the gas was then flowed back to the pump. The amount of adsorbed methane within the shale sample after a desorption step can be obtained by:

$$n_{\text{des}}^{Gibbs-i} = n_{total-before}^{i+1} - n_{outflow}^{i} - n_{void} - n_{poro} \tag{6}$$

Where $n_{\text{des}}^{Gibbs-i}$ is the amount of adsorbed methane gas after the desorption experiment to pressure P_i, $n_{total-before}^{i+1}$ is the total amount of the gas in the void and sample before the desorption experiment to pressure P_{i+1}, $n_{outflow}^{i}$ is the amount flowed from the sample and system and captured by the ISCO pump.

2.4.4 Strain

During each pressure step of the helium porosity or methane adsorption, the displacement measurement from the LDVTs are recorded simultaneously. Axial strain is calculated from sample's length change before and after the gas injection:

$$\varepsilon_{\text{axial}} = \left(L_{\text{after}} - L_{\text{before}}\right)/L - \varepsilon'_{\text{axial}} \tag{7}$$

Where $\varepsilon_{\text{axial}}$ is the axial strain of the shale sample, L_{after} is the sample length after gas injection, L_{before} is the sample Length before gas injection, L is the sample length, and $\varepsilon'_{\text{axial}}$ the deformation error, which is calibrated using the steel sample.

Radial strain is calculated from the relative deformation of the sample's perimeter before and after the gas injection.

$$\varepsilon_{\text{Radial}} = \left(l_{\text{after}} - l_{\text{before}}\right)/\pi D - \varepsilon'_{\text{radial}} \tag{8}$$

Where $\varepsilon_{\text{Radial}}$ is the radial strain of the shale sample, l_{after} is the sample perimeter after

gas injection, l_{before} is the sample perimeter before gas injection, D is the diameter of the sample, and ε'_{radial} is the deformation error, which is calibrated using the steel sample.

Since the samples in this work were collected from outcrop, the experimental conditions was determined based on the drilling information of the shale gas well Chang 1, which is close to the sampling site. From the Chang 1 drilling results, the Niutitang formation starts at 535m, the black shale and carbonaceous shale starts at 742m and the bottom is located at 1344m (He et al., 2015; Lin et al., 2014). Based on the overburden density and ratio of vertical stress and horizontal stress, horizontal stress of Niutitang shale reservoir is approximately 20 MPa, so the hydrostatic pressure of 20 MPa was used in this work. All the experiments were carried out at a constant hydrostatic pressure of 20 MPa and temperature of 25 °C.

3. Experimental results

3.1 Pore structure and size distribution characteristics

The surface areas, pore volume, and pore size distribution calculated from the N_2 adsorption isotherms at 77K for the two samples are showed in Fig. 3. Pore size ranges from 1.69 nm to 58.11 nm for Sample1 and from 1.69 nm to 50.69 nm for Sample2. Pores with the width less than 8 nm are the main contributor to pore volume of the shale (Fig. 3a). The surface areas are predominantly dominated by pores with the width less than 6 nm (Fig. 3a). The increasing trends of pore volume and surface areas become slower with increasing pore width (Fig. 3b). The BET surface area is 6.338 m^2/g for Sample1and 7.6 m^2/g for Sample2. The average pore width is 6.53 nm for Sample1 and 5.82 nm for Sample2.

Figure 4 shows the typical mineral composition and microstructure of the shale observed by SEM. Microstructure of Sample1 shown in Fig. 4a is similar to that of Sample2 shown in Fig. 4b. Detailed structures of Sample1 are shown in following figures (from Fig. 4c to Fig. 4f). Similar structures can be observed in Sample2; however they are not presented to avoid repetition. Boundaries of mineral grain is indistinct in the shales. Quartz and feldspar are granular and pyrite is locally concentrated. In spite of the significant proportion, the size change of these brittle minerals under gas pressure may be minor due to the high stiffness. Pores developed between inorganic minerals, between inorganic minerals and organic matter, and in organic matters were found in the shales. Pore size ranges from nanometers to microns. There is a larger quantity of nano-sized pores and they are mainly developed in organic matter (Fig. 4c). Pores in inorganic minerals were also observed (Fig. 4d). Nanometer fractures developed between brittle mineral grains were observed (Fig. 4e). Clay minerals are mainly strip-shaped and they are also found interbedded with organic matter in the shale as shown in Fig. 4f. Nanometer fractures also exist between lamellar structures of the mixture of clay mineral and organic matter. Bedding structure of clay mineral may be the cause of shale property anisotropy.

3.2 Helium porosity

Helium porosity measurement was carried out at five pressure steps. The gas pressure was increased from 0 to 10 MPa at an interval of 2 MPa. The results are shown in Fig. 5.

Although organic-rich shale is tightly packed, the pore volume in the shale increases as the gas pressure increases, at constant hydrostatic pressure of 20 MPa. The helium porosity increases from 0.072 to 0.089 for Sample1 and 0.084 to 0.098 for Sample2.

3.3 Methane adsorbed gas and free gas

The same pressure steps were used in the methane adsorption measurement. Desorption steps were performed from 10 to 2 MPa at the same interval as 2 MPa to investigate the sorption hysteresis. The amount of methane adsorption at different gas pressure is calculated using equations described above and the results are shown in Fig. 6. Langmuir model is applied to describe the adsorption experimental data and the Langmuir isotherm is also plotted in Fig. 6. The Langmuir model is (Langmuir, 1918):

$$n_a = \frac{V_L P}{P + P_L} \tag{9}$$

Where n_a is adsorbed volume per unit mass of shale, V_L is the Langmuir volume, P is gas pressure, P_L is Langmuir pressure. The Langmuir volume is 5.33 m^3/t and the Langmuir pressure is 6.01 MPa for the methane sorption isotherms on this shale based on all the adsorption and desorption points for Sample1 and they are 4.08 m^3/t and 4.02 MPa for Sample2.

Hysteresis between the methane adsorption and desorption isotherms are observed. These adsorption results are consistent with the results from literature (eg., Chareonsuppanimit et al., 2012). Desorption experimental data is not in agreement with Langmuir model because of the existence of hysteresis.

Besides the adsorbed gas, free gas in the shale matrix is another contributor to the total gas content. Free gas can be calculated by:

$$n_f = \rho_g \left(V_\phi - \frac{n_a}{\rho_a} \right) \tag{10}$$

Where n_f is the amount of matrix free gas per unit mass of shale, ρ_g is gas density in the matrix pores, V_ϕ is the helium pore volume per unit mass of shale, ρ_a is the adsorbed phase density. $\frac{n_a}{\rho_a}$ is the volume occupied by the adsorbed gas, which becomes important at high pressures thus needs to be deducted for free gas (Pan and Connell, 2015).

Total gas is the summation of the free gas and adsorbed gas and the results of total gas are also shown in Fig. 6. It can also be seen from Fig. 6 that at pressure of 2 MPa, the free gas is about 24% of the total gas for the Sample1 and 34% for the Sample2, however, when the pressure is 10 MPa, the free gas is about 53% of the total gas for the Sample1 and 58% for the Sample2.

3.4 Strain Results

The strain of the shale caused by gas injection can be calculated using the equations described earlier. Swelling strain is represented by a positive value in this paper. Although in rock mechanics, compressive deformation is represented by a positive value, we use positive value to represent swelling because the swelling is more directly related to strain increase and this is widely accepted in the literature for gas induced coal swelling. All the results are summarized in Table 2.

Fig. 7 shows the relationship between the amount of gas uptake by the shale and the strain results caused by injecting helium and methane, respectively, for both samples. As the curves at the different pressure steps are similar, only the results for the pressure step from 0 to 2 MPa are illustrated. The amount of gas uptake here means the amount of gas in the shale sample including adsorbed gas and free gas. It is considered that there is no adsorbed gas for helium injection, thus the helium uptake is free gas only. It should be noted that in Fig. 7 the gas uptake volume is the volume at its final pressure of each pressure step. At constant hydrostatic pressure of 20 MPa, when gas was injected, the pore space in the shale was filled with gas. Thus, the effective stress on the shale is reduced, making the shale to expand. The strain and gas uptake show a positively correlated relationship.

Fig. 8 shows the strain with respect to square root of time for both samples. As the curves at the different pressure steps are similar, only the results for the pressure step from 0 to 2 MPa are illustrated. From the figure, it can be seen that both the strain change and the gas uptake show a two stage process: the strain and gas uptake both show a rapid increase with respect to time followed by a much slower and longer period in which both strain and gas uptake changes slightly. These demonstrated that the strain and gas uptake both are related to the diffusion process of gas in pores of different sizes in shale (Yuan et al., 2014b). Moreover, the figure also shows that strains induced by methane are larger than that induced by helium. To further compare the difference between the axial and radial strains with helium and CH_4 injection for the same pressure steps, the swelling strain step change of different gases in Table 2 were analyzed. From the analysis, it can be concluded that the strain difference between helium and CH_4 is largest when pressure is from 0 to 2 MPa. The difference gradually reduces as pressure goes higher. It can also be seen that there is strain anisotropy with more strain at the radial direction, which is perpendicular to bedding.

Fig. 9 compares the strain measurement for CH_4 pressure increase and decrease cycles for both samples. As the curves at the different pressure steps are similar, only the results for the pressure step from 6 to 8 and from 8 to 6 MPa are illustrated. The terms of adsorption and desorption are not used here because a significant amount of gas is stored in shale as free gas phase. The negative strain in the pressure decrease cycle means strain decreases; however, in order to compare with the strain in the pressure increase cycle, the negative strain is converted to positive for easy comparison. It should be also noted that the final pressure is

different between pressure increase and decrease cycles in Fig. 9. The final pressure is 8 MPa for the pressure increase cycle while it is 6 MPa for the pressure decrease cycle, making the direct comparison difficult. Especially for the results in Table 2, the strain change is much larger when pressure is from 2 to 0 MPa. Thus calculated strain hysteresis is carried out and analyzed in the discussion section below.

The equilibrium strain in Helium and methane with respect to pressure is plotted in Fig. 10. The equilibrium strain is calculated by accumulating the strain change at each pressure step to the target pressure. It can be seen from the figure that the strain change caused by Helium is a linear function of pressure, but the strain change caused by methane does not change linearly with pressure. The strain in methane is double the strain in helium, suggesting an adsorption induced swelling, which is detailed in discussion.

4. Discussion

4.1 Adsorption induced swelling strain

The shale strain change caused by methane injection can be attributed to two effects: the poroelasticity effect and the adsorption induced swelling effect:

$$\varepsilon_t = \varepsilon_p + \varepsilon_a \tag{11}$$

Where ε_t is the total measured strain in methane, ε_p is the strain caused by poroelasticity, ε_a is the adsorption induced swelling strain. By subtracting the poroelsticity caused strain, which is obtained from the helium strain results, from the overall methane strain, the adsorption-induced shale swelling strain can be obtained. The adsorption induced swelling strain is shown in Fig. 10. From the figure, it can be seen that the adsorption induced swelling strain can be visually identified as a Langmuir-like curve, which is often used to empirically describe the gas adsorption induced coal swelling (Cui and Bustin, 2005; Harpalani and Schraufnagel, 1990; Shi and Durucan, 2004):

$$\varepsilon_a = \frac{\varepsilon_L P}{P + P_L} \tag{12}$$

The matrix strain ε_L is 0.104% and the Langmuir pressure P_L for strain is 3.81MPa for Sample1 and they are 0.134% and 5.13MPa for Sample2.

Figure 10 also shows that adsorption induced shale swelling has a noticeable hysteresis between the adsorption and desorption cycles. The hysteresis ratio increases from 4% at 8MPa to 12% at 2MPa for Sample1 and from 2% to 23% with the same pressure change for Sample2, meaning that hysteresis becomes strong when the pressure goes lower. Swelling hysteresis should be closely related to the adsorption/desorption hysteresis.

It is also naturally to correlate the adsorption induced swelling strain with the amount of adsorption (Shi and Durucan, 2005). As can be seen from Fig. 11, the adsorption induced

swelling is almost linear to the adsorption amount, which is also observed from gas adsorption induced coal swelling at low to moderate pressures. The swelling strain of gas shale is an order of magnitude lower than that measured on coal at the similar gas pressure by other authors (Ceglarska-Stefaríska, 1994; Pan et al., 2010; Staib et al., 2014).

Since there is no other adsorption induced swelling measurement on shales, comparison is made with that on coals. Fig. 12 compares the adsorption induced swelling strain and absolute adsorption amount for coal and gas shale. Literature data also include N_2 and CO_2 adsorption induced coal swelling (Bustin, 2004; Day et al., 2008; Levine, 1996). Swelling measurements on organic carbon and illite by Heller and Zoback (2014) were also included in the figure. It can be seen from Fig. 12, gas adsorption induced swelling strain for this shale is in line with that for coals and organic carbon, however, the swelling strain of illite deviates from the rest of the results.

4.2 Anisotropic strain

The experimental results also show that the sample has a slight anisotropy between the radial and axial directions. Radial direction is perpendicular to bedding direction, which has higher strain and adsorption strain. Axial and radial strain of the shale samples in the helium and methane, adsorption induced swelling strain are shown in Fig. 13. From the helium results, the strain anisotropy ratio, which is obtained through dividing radial strain by axial strain, increases from 1.03 at 2 MPa to 1.2 at 10 MPa for Sample1 and they are 1.24 and 1.28 at respective pressures for Sample2. The reason for this increase could be because that the shale is not perfect linearly elastic at this pressure region.

The strain anisotropy ratio for the shale in methane is from 1.02 at 2 MPa to 1.1 at 10 MPa for Sample1 and they are 1.04 and 1.13 at respective pressures for Sample2, for the methane pressure decrease cycle, the strain anisotropy ratio is also in the similar trend. Adsorption induced coal swelling also shows a slight anisotropy as shown in Fig. 13. These anisotropic strain results are the same as the strain results on coals (Day et al., 2008) and could be possibly because of the shale structure difference between the different directions as well as anisotropy in pore structure and mechanical properties (Pan and Connell, 2011).

5. Conclusions

An experimental study of shale strain change with gas injection was carried out for two shale samples from the Niutitang formation in Northwest Hunan province, China. Both helium, a non-adsorbing gas, and methane, an adsorbing gas, were used. Methane adsorption measurement was also carried out simultaneously with the strain measurement. All the measurements were conducted at constant hydrostatic pressure of 20 MPa and constant temperature of 25 ^{o}C. The gas adsorption induced shale swelling is identified and its relationship with adsorption amount is studied. The following conclusions can be made from

this study:

(1) The gas adsorption induced volumetric swelling strain is in the magnitude of 0.1% at methane pressure of 10 MPa, which is about one magnitude lower than the methane adsorption induced swelling for coal. Nevertheless, this is in line with the gas adsorption induced coal swelling, as the adsorption amount is also one magnitude lower for the shale samples studied.

(2) The adsorption induced swelling strain shows a Langmuir-like curve with respect to gas pressure and shows a linear relationship with methane adsorption amount. Gas adsorption induced swelling is about the same magnitude of the strain caused by poroelasticity for the shale samples studied.

(3) All strains show slight anisotropy for the samples studied in this work, with the strains larger at the direction perpendicular to the bedding. Gas adsorption induced shale swelling results also show slight hysteresis for the adsorption and desorption cycles and the adsorption hysteresis is also evident.

Acknowledgement

Funding support from National Natural Science Foundation of China under Grant no.11232024 is acknowledged. Authors also thank Xiwei Zhang, Yuanhui Li and Chengxiang Yang for their help on the development of the testing system.

References

Bustin, R.M., 2004. Acid gas sorption by British Columbia coal: implications for permanent disposal of acid gas in deep coal seams and possible co-production of methane. Final report OGC funding agreement 2000-16, The University of British Columbia (http://scek.ca/documents/scek/Final_Reports/d-ET-Com-UBC-2000-16-Rep.pdf, accessed 10 December 2014).

Ceglarska-Stefaríska, G., 1994. Effect of Gas Pressure in Methane Induced Swelling on the Porous Structure of Coals, in: J. Rouquerol, F.R.-R.K.S.W.S., Unger, K.K. (Eds.), Studies in Surface Science and Catalysis. Elsevier, pp. 671-677.

Chalmers, G.R.L., Ross, D.J.K., Bustin, R.M., 2012. Geological controls on matrix permeability of Devonian Gas Shales in the Horn River and Liard basins, northeastern British Columbia, Canada. International Journal of Coal Geology 103, 120-131.

Chareonsuppanimit, P., Mohammad, S.A., Robinson Jr, R.L., Gasem, K.A.M., 2012. High-pressure adsorption of gases on shales: Measurements and modeling. International Journal of Coal Geology 95, 34-46.

Cui, X., Bustin, R.M., 2005. Volumetric strain associated with methane desorption and its impact on coalbed gas production from deep coal seams. Aapg Bulletin 89, 1181-1202.

Day, S., Fry, R., Sakurovs, R., 2008. Swelling of Australian coals in supercritical CO2. International Journal of Coal Geology 74, 41-52.

Fitzgerald, J., Pan, Z., Sudibandriyo, M., Robinson Jr, R., Gasem, K., Reeves, S., 2005. Adsorption of methane, nitrogen, carbon dioxide and their mixtures on wet Tiffany coal. Fuel 84, 2351-2363.

Gasparik, M., Bertier, P., Gensterblum, Y., Ghanizadeh, A., Krooss, B.M., Littke, R., 2014. Geological controls on the methane storage capacity in organic-rich shales. International Journal of Coal Geology 123, 34-51.

Guo, S., 2013. Experimental study on isothermal adsorption of methane gas on three shale samples from Upper Paleozoic strata of the Ordos Basin. Journal of Petroleum Science and Engineering 110, 132-138.

Harpalani, S., Schraufnagel, A., 1990. Measurement of parameters impacting methane recovery from coal seams. International Journal of Mining and Geological Engineering 8, 369-384.

Hartwig, A., Schulz, H.-M., 2010. Applying classical shale gas evaluation concepts to Germany—Part I: The basin and slope deposits of the Stassfurt Carbonate (Ca2, Zechstein, Upper Permian) in Brandenburg. Chemie der Erde - Geochemistry 70, Supplement 3, 77-91.

He, W., Zhang, J., Li, L., Pu, H., 2015. Lower Cambrian series Niutitang Formation shale gas reservoir characteristics in Changye No.1 well, northwestern Hunan. Coal Geology of China 27, 31-39.

Heller, R., Zoback, M., 2014. Adsorption of methane and carbon dioxide on gas shale and pure mineral samples. Journal of Unconventional Oil and Gas Resources 8, 14-24.

Hill, D.G., Nelson, C., 2000. Gas productive fractured shales: an overview and update. Gas Tips 6, 4-13.

Hou, Y., He, S., Yi, J., Zhang, B., Chen, X., Wang, Y., Zhang, J., Cheng, C., 2014. Effect of pore structure on methane sorption potential of shales. Petroleum Exploration and Development 41, 272-281.

Labani, M.M., Rezaee, R., Saeedi, A., Hinai, A.A., 2013. Evaluation of pore size spectrum of gas shale reservoirs using low pressure nitrogen adsorption, gas expansion and mercury porosimetry: A case study from the Perth and Canning Basins, Western Australia. Journal of Petroleum Science and Engineering 112, 7-16.

Langmuir, I., 1918. The adsorption of gases on plane surfaces of glass, mica and platinum. Journal of the American Chemical society 40, 1361-1403.

Levine, J.R., 1996. Model study of the influence of matrix shrinkage on absolute permeability of coal bed reservoirs. Geological Society, London, Special Publications 109, 197-212.

Lin, T., Zhang, J., Li, B., Yang, S., He, W., Tang, X., Ma, L., Pei, S., 2014. Shale gas accumulation conditions and gas-bearing properties of the Lower Cambrian Niutitang Formation in Well Changye 1, northwestern Hunan. Shiyou Xuebao/Acta Petrolei Sinica 35, 839-846.

Loucks, R.G., Reed, R.M., Ruppel, S.C., Jarvie, D.M., 2009. Morphology, Genesis, and Distribution of Nanometer-Scale Pores in Siliceous Mudstones of the Mississippian Barnett Shale. Journal of Sedimentary Research 79, 848-861.

Lu, X.-C., Li, F.-C., Watson, A.T., 1995. Adsorption measurements in Devonian shales. Fuel 74, 599-603.

Nie, H., Zhang, J., Li, Y., 2011. Accumulation conditions of the Low Cambrain shale gas in the Sichuan Basin ans its periphery. Acta Petrolei Sinica 32, 960-967.

Pan, Z., Connell, L.D., 2007. A theoretical model for gas adsorption-induced coal swelling. International Journal of Coal Geology 69, 243-252.

Pan, Z., Connell, L.D., 2011. Modelling of anisotropic coal swelling and its impact on permeability behaviour for primary and enhanced coalbed methane recovery. International Journal of Coal Geology 85, 257-267.

Pan, Z., Connell, L.D., 2015. Reservoir simulation of free and adsorbed gas production from shale. Journal of Natural Gas Science and Engineering 22, 359-370.

Pan, Z., Connell, L.D., Camilleri, M., Connelly, L., 2010. Effects of matrix moisture on gas diffusion and flow in coal. Fuel 89, 3207-3217.

Ross, D.J.K., Marc Bustin, R., 2009. The importance of shale composition and pore structure upon gas storage potential of shale gas reservoirs. Marine and Petroleum Geology 26, 916-927.

Shi, J.-Q., Durucan, S., 2005. A model for changes in coalbed permeability during primary and enhanced methane recovery. SPE Reservoir Evaluation & Engineering 8, 291-299.

Shi, J., Durucan, S., 2004. Drawdown induced changes in permeability of coalbeds: a new interpretation of the reservoir response to primary recovery. Transport in porous media 56, 1-16.

Soroush, H., Rasouli, V., Tokhmechi, B., 2010. A data processing algorithm proposed for identification of breakout zones in tight formations: A case study in Barnett gas shale. Journal of Petroleum Science and Engineering 74, 154-162.

Staib, G., Sakurovs, R., Gray, E.M., 2014. Kinetics of coal swelling in gases: Influence of gas pressure, gas type and coal type. International Journal of Coal Geology 132, 117-122.

Tan, J., Weniger, P., Krooss, B., Merkel, A., Horsfield, B., Zhang, J., Boreham, C.J., Graas, G.v., Tocher, B.A., 2014. Shale gas potential of the major marine shale formations in the Upper Yangtze Platform, South China, Part II: Methane sorption capacity. Fuel 129, 204-218.

Tian, H., Pan, L., Zhang, T., Xiao, X., Meng, Z., Huang, B., 2015. Pore characterization of organic-rich Lower Cambrian shales in Qiannan Depression of Guizhou Province, Southwestern China. Marine and Petroleum Geology 62, 28-43.

Wang, C., Xiao, z., Yang, R., Feng, T., Wang, Q., Huang, Y., Chen, Y., Ning, B., 2014. Study on the gas production material base of shale gas in Lower Cambrian Niutitang Formation, northwestern Hunan. China Mining Magazine 23, 66-70.

Weniger, P., Kalkreuth, W., Busch, A., Krooss, B.M., 2010. High-pressure methane and carbon dioxide sorption on coal and shale samples from the Paraná Basin, Brazil. International Journal of Coal Geology 84, 190-205.

Xiao, Z., Yang, R., Feng, T., Cao, Y., Wang, Q., Yang, T., Wang, C., Deng, Y., 2012. Reservoir-forming conditions and exploration potential of shale gas in Low Cambrain Niutitang Formation, Northwestern Hunan. Journal of Hunan University of Science & Technology (Natural Science Edition) 27, 50-50.

Yu, W., Sepehrnoori, K., 2014. Simulation of gas desorption and geomechanics effects for unconventional gas reservoirs. Fuel 116, 455-464.

Yuan, W., Li, X., Pan, Z., Connell, L.D., Li, S., He, J., 2014a. Experimental investigation of interactions between water and a lower Silurian Chinese shale. Energy & Fuels 28, 4925-4933.

Yuan, W., Pan, Z., Li, X., Yang, Y., Zhao, C., Connell, L.D., Li, S., He, J., 2014b. Experimental study and modelling of methane adsorption and diffusion in shale. Fuel 117, Part A, 509-519.

Zhang, L., Guo, J., Jiao, P., Zhang, Z., 2014. Accumulation conditions and resource potential of shale gas in Lower Cambrian Niutitang formation, northwestern Hunan. Zhongnan Daxue Xuebao (Ziran Kexue Ban)/Journal of Central South University (Science and Technology) 45, 1163-1173.

Zhang, T., Ellis, G.S., Ruppel, S.C., Milliken, K., Yang, R., 2012. Effect of organic-matter type and thermal maturity on methane adsorption in shale-gas systems. Organic Geochemistry 47, 120-131.

Tables

Table 1. TOC, $R_{o,max}$ and mineral compositions of the shale samples

Sample ID	Mineral compositions (%)				TOC (%)	$R_{o,max}$ (%)
	Quartz	Feldspar	Pyrite	Clay minerals		
Sample1	54.74	11.38	1.96	25.18	6.74	2.42
Sample2	56.44	10.12	1.76	24.51	7.17	2.47

Table 2. Strain step change in different gases

		Strain (%)	Pressure step (MPa)				
			0–2	2–4	4–6	6–8	8–10
Sample1	He	Axial strain	0.0035	0.0037	0.0038	0.0048	0.0034
		Radial strain	0.0036	0.0042	0.0043	0.0052	0.0057
		Volumetric strain	0.0108	0.0121	0.0124	0.0152	0.0147
	CH_4 pressure increase	Axial strain	0.0155	0.0087	0.0070	0.0069	0.0059
		Radial strain	0.0160	0.0095	0.0079	0.0080	0.0071
		Volumetric strain	0.0475	0.0277	0.0228	0.0228	0.0201
	CH_4 Pressure decrease	Axial strain	-0.0107	-0.0079	-0.0062	-0.0066	-0.0050
		Radial strain	-0.0136	-0.0098	-0.0086	-0.0073	-0.0060
		Volumetric strain	-0.0380	-0.0275	-0.0235	-0.0211	-0.0169
Sample2	He	Axial strain	0.0033	0.0028	0.0035	0.0030	0.0032
		Radial strain	0.0041	0.0036	0.0040	0.0035	0.0042
		Volumetric strain	0.0116	0.0100	0.0115	0.0100	0.0115
	CH_4 pressure increase	Axial strain	0.0177	0.0071	0.0060	0.0085	0.0052
		Radial strain	0.0184	0.0084	0.0074	0.0097	0.0065
		Volumetric strain	0.0544	0.0238	0.0207	0.0278	0.0182
	CH_4 Pressure decrease	Axial strain	-0.0057	-0.0074	-0.0069	-0.0050	-0.0048
		Radial strain	-0.0063	-0.0088	-0.0075	-0.0060	-0.0059
		Volumetric strain	-0.0183	-0.0251	-0.0219	-0.0170	-0.0165

Figures

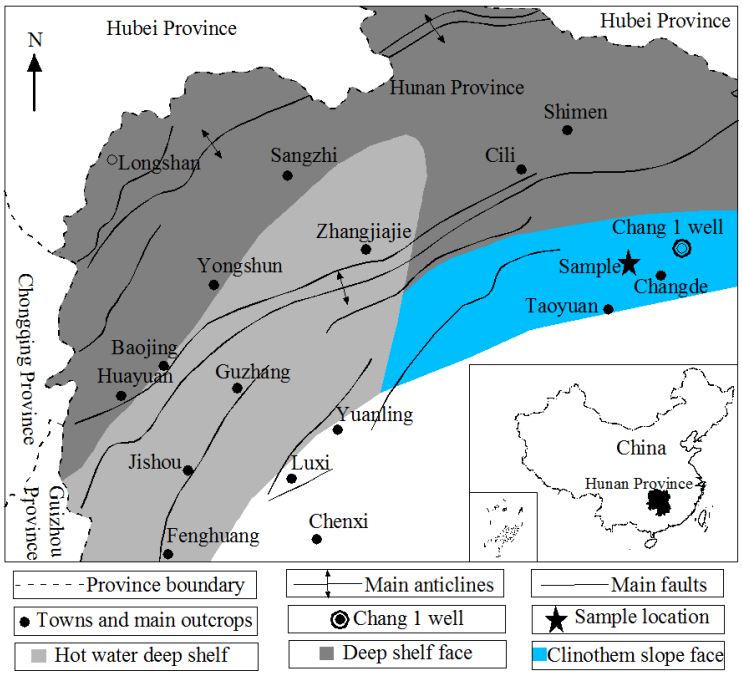

Fig. 1. The location of Hunan province in China, the main geological structures and the sample location in northwest of Hunan province

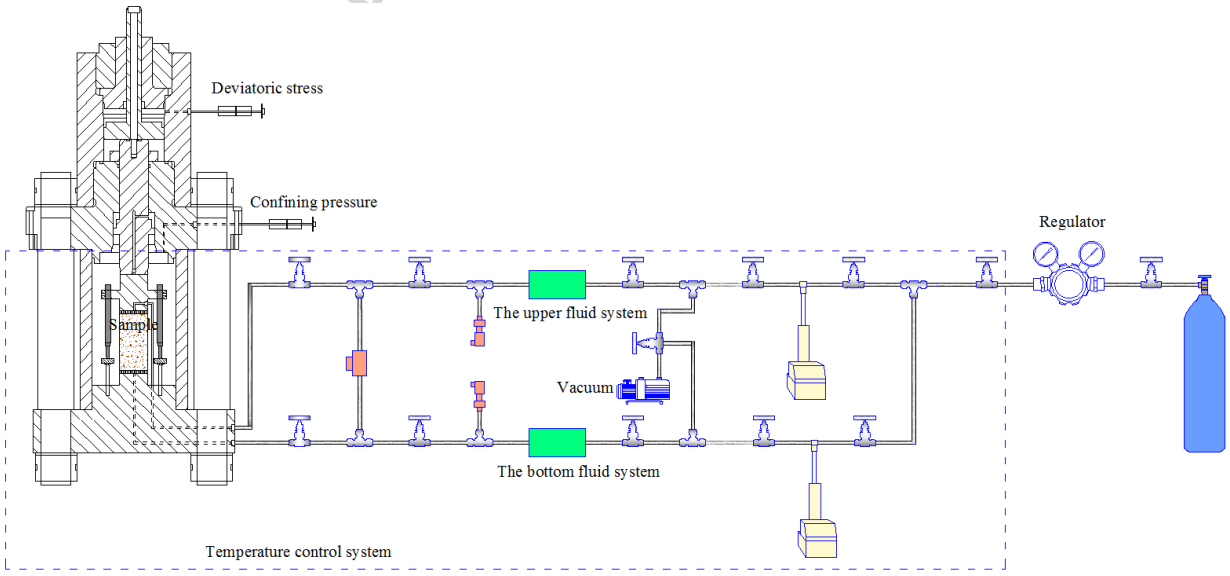

Fig. 2. Schematic diagram of the experimental set up

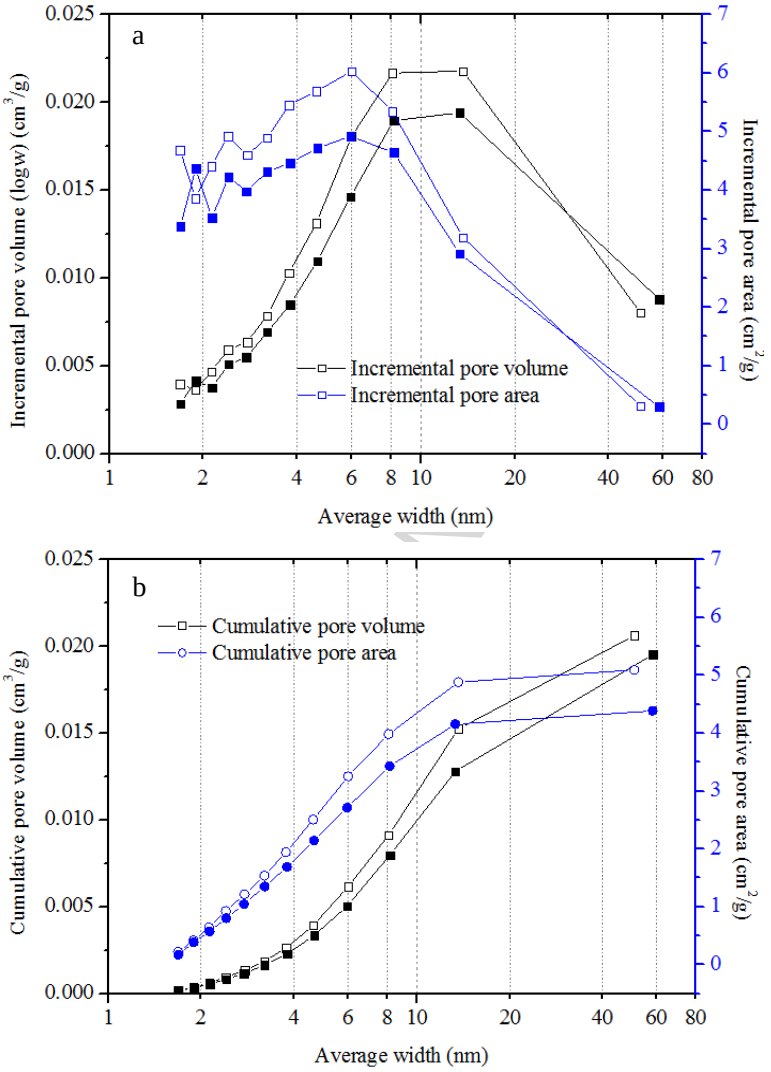

Fig. 3. The relationship of surface area and pore volume with pore size (Solid symbol: Sample1; Empty symbol: Sample2)

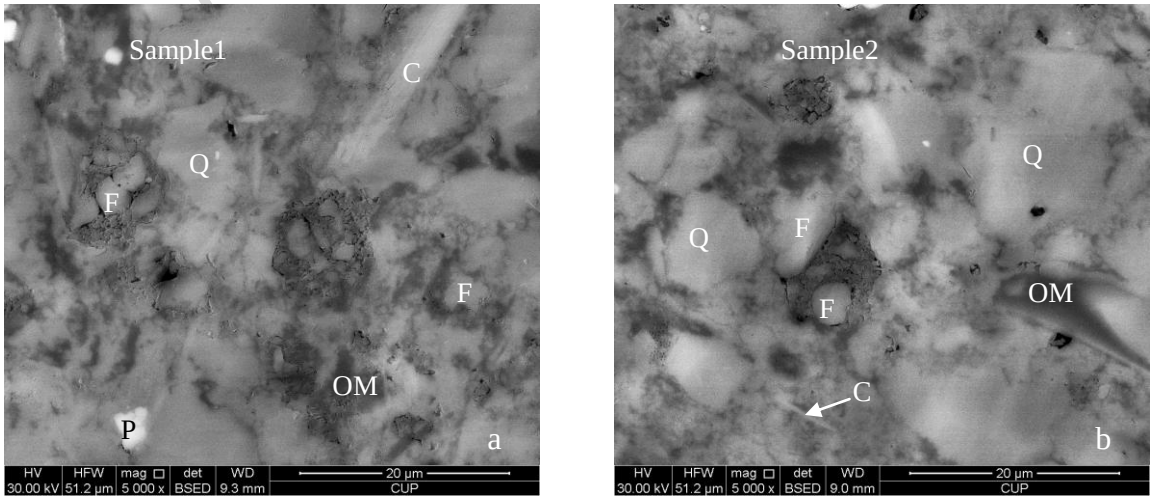

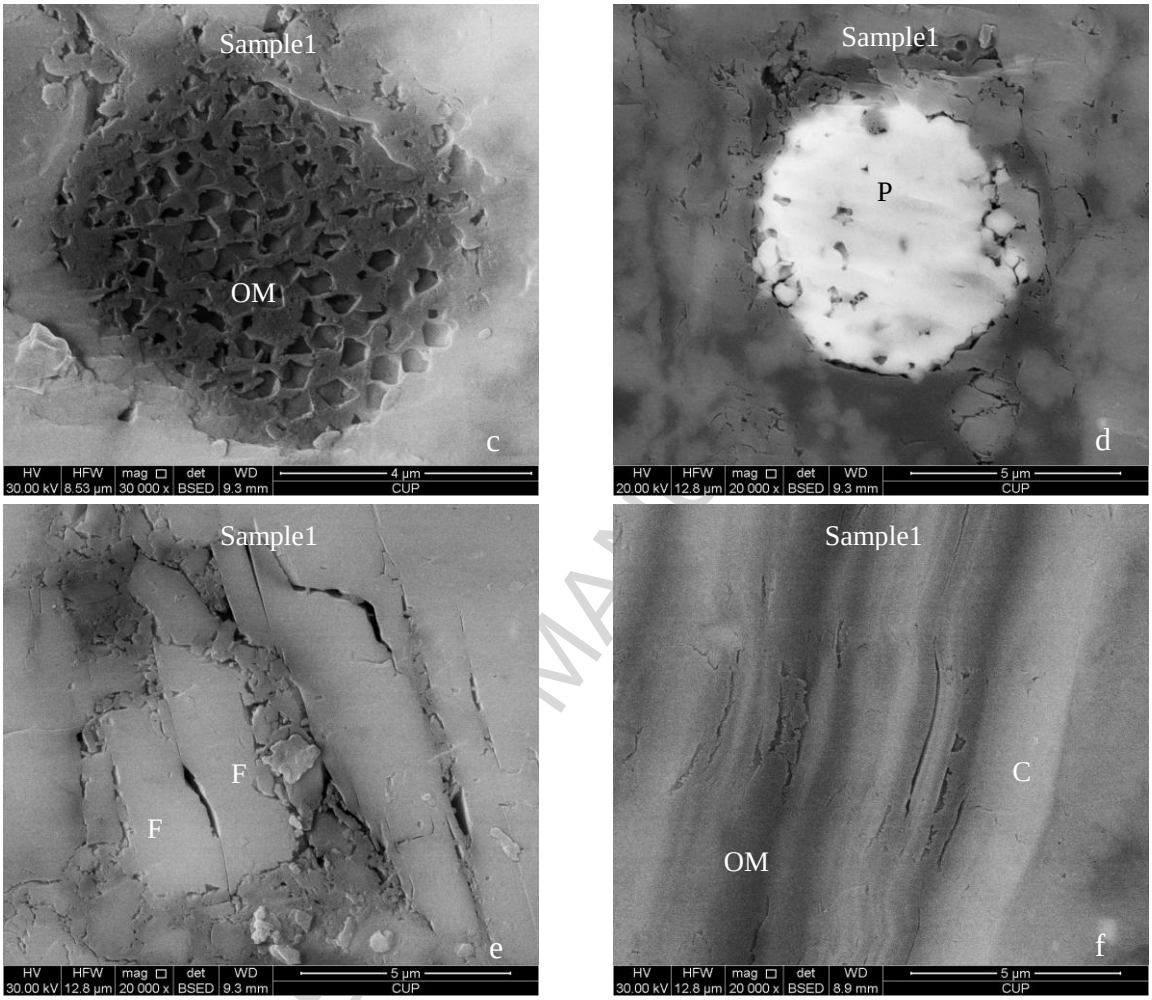

Fig. 4. The typical mineral composition and microstructure of the shale (C: clay; Q: quartz; F: feldspar; P: pyrite; OM: organic matter)

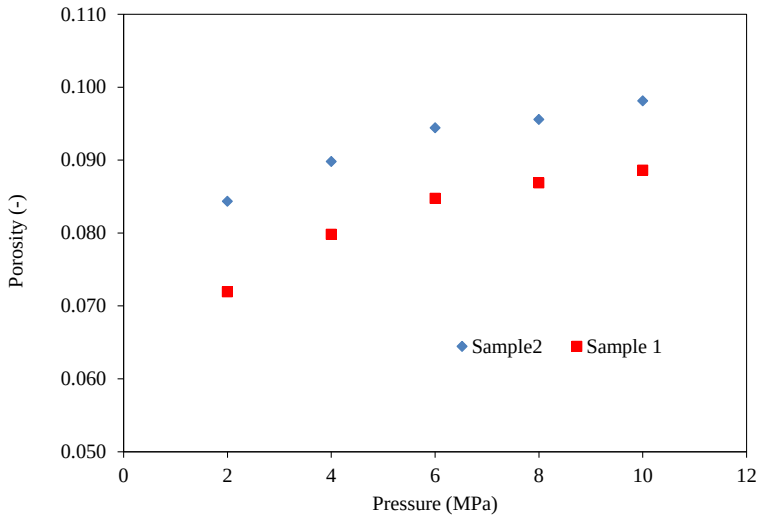

Fig. 5. Helium porosity with respect to gas pressure at constant hydrostatic pressure

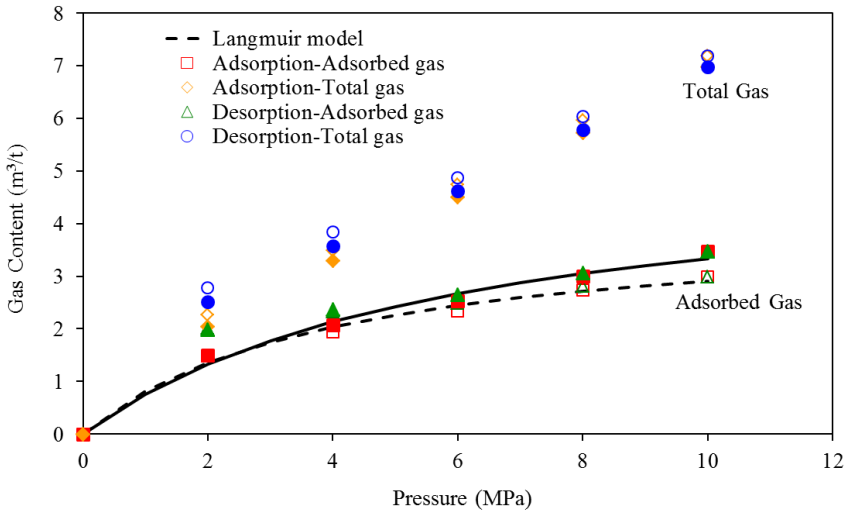

Fig. 6. Total gas, CH_4 isotherms and Langmuir model fit (Solid symbol: Sample1; Empty symbol: Sample2)

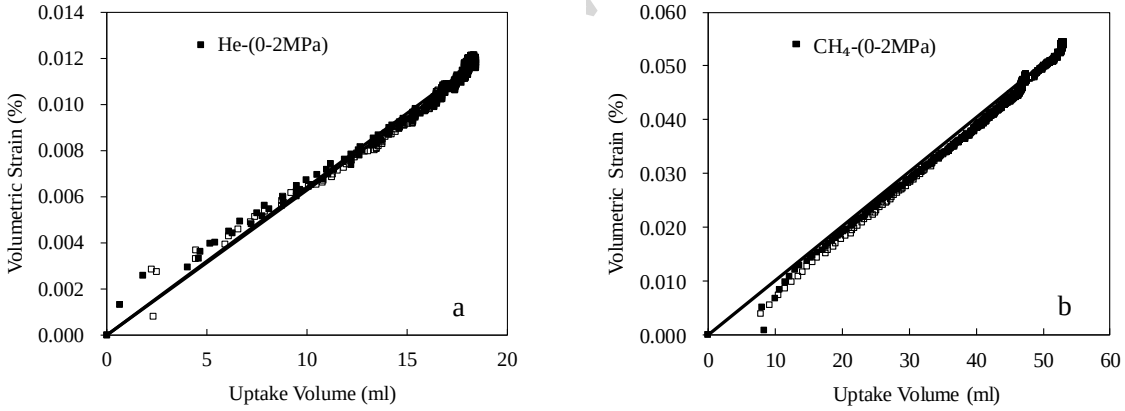

Fig. 7. The relationship between gas uptake volume and volumetric strain (Solid symbol: Sample1; Empty symbol: Sample2)

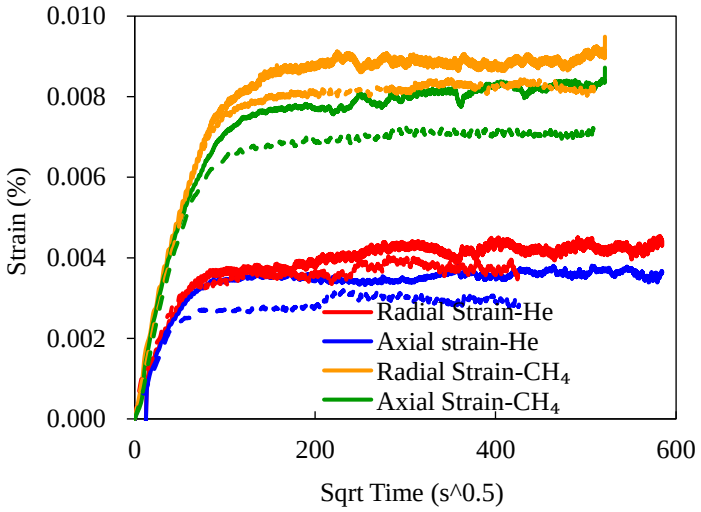

Fig. 8. The evolution of strain during gas injection with pressure from 0 to 2 MPa (Soild line: Sample1; Dashed line: Sample2)

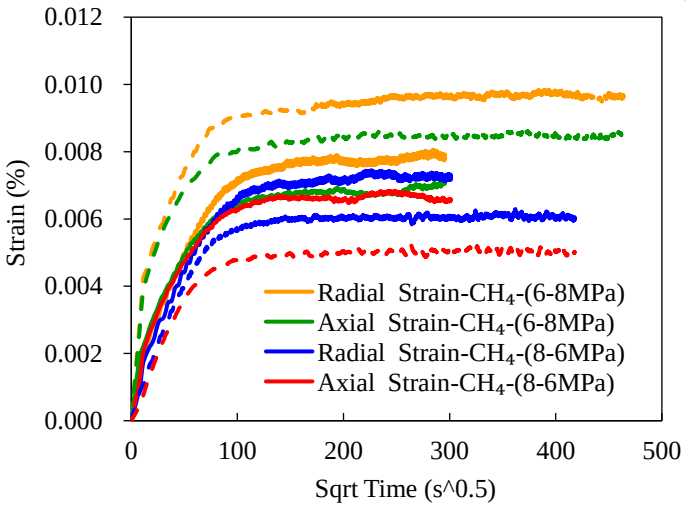

Fig. 9. The evolution of strain during pressure increase and decrease cycles (Soild line: Sample1; Dashed line: Sample2)

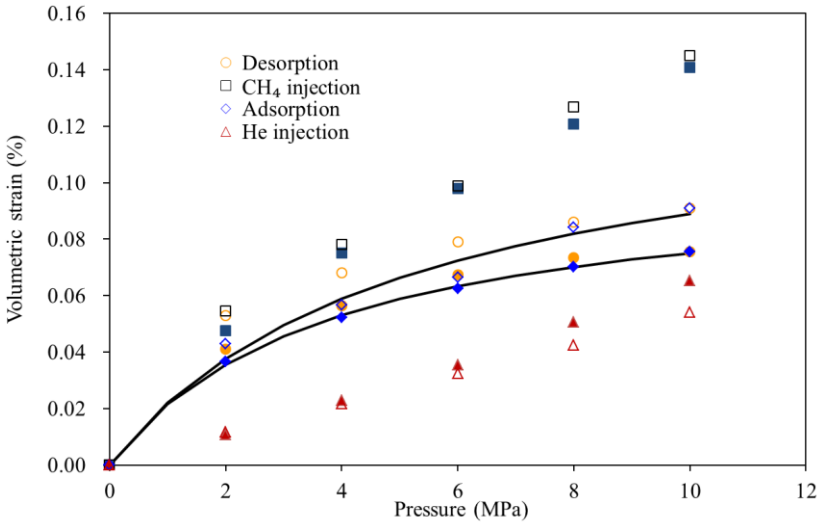

Fig. 10. Different components of volumetric strain of the shale samples (Solid symbol: Sample1; Empty symbol: Sample2)

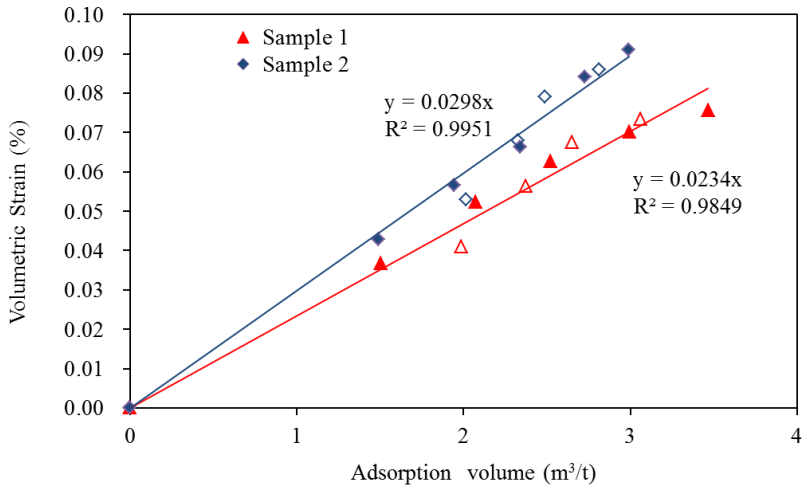

Fig. 11. Relationship between adsorbed amount and its induced shale swelling (solid symbol: pressure increase cycle; empty symbol: pressure decrease cycle)

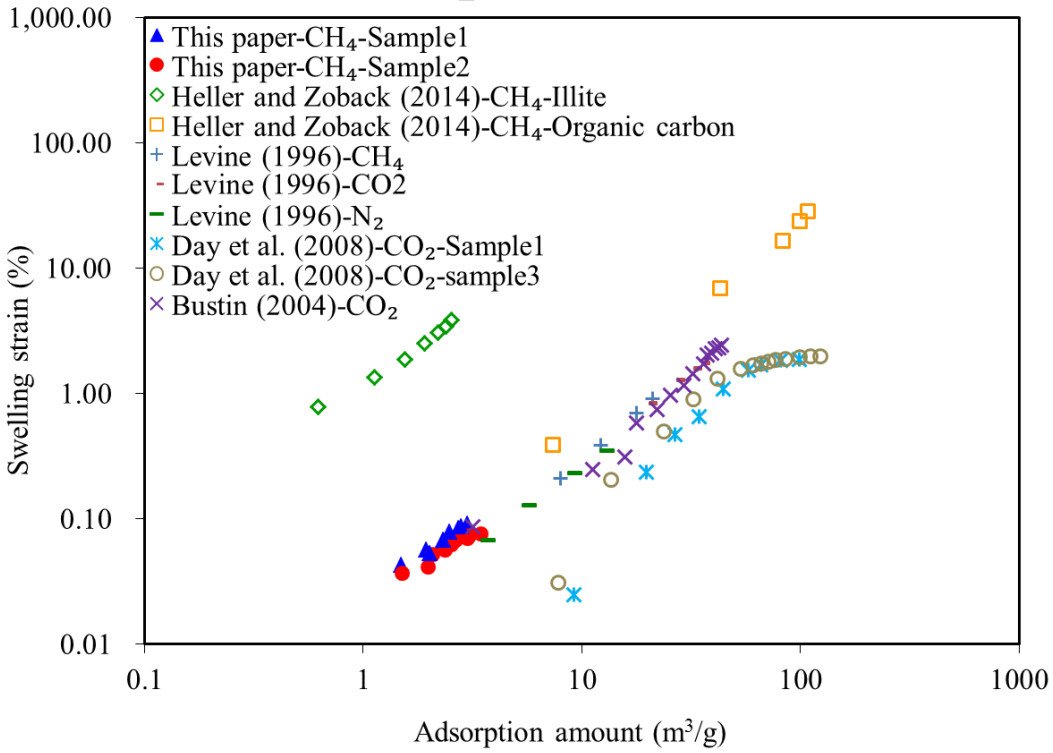

Fig. 12. Comparison of adsorption induced swelling strain with literature data

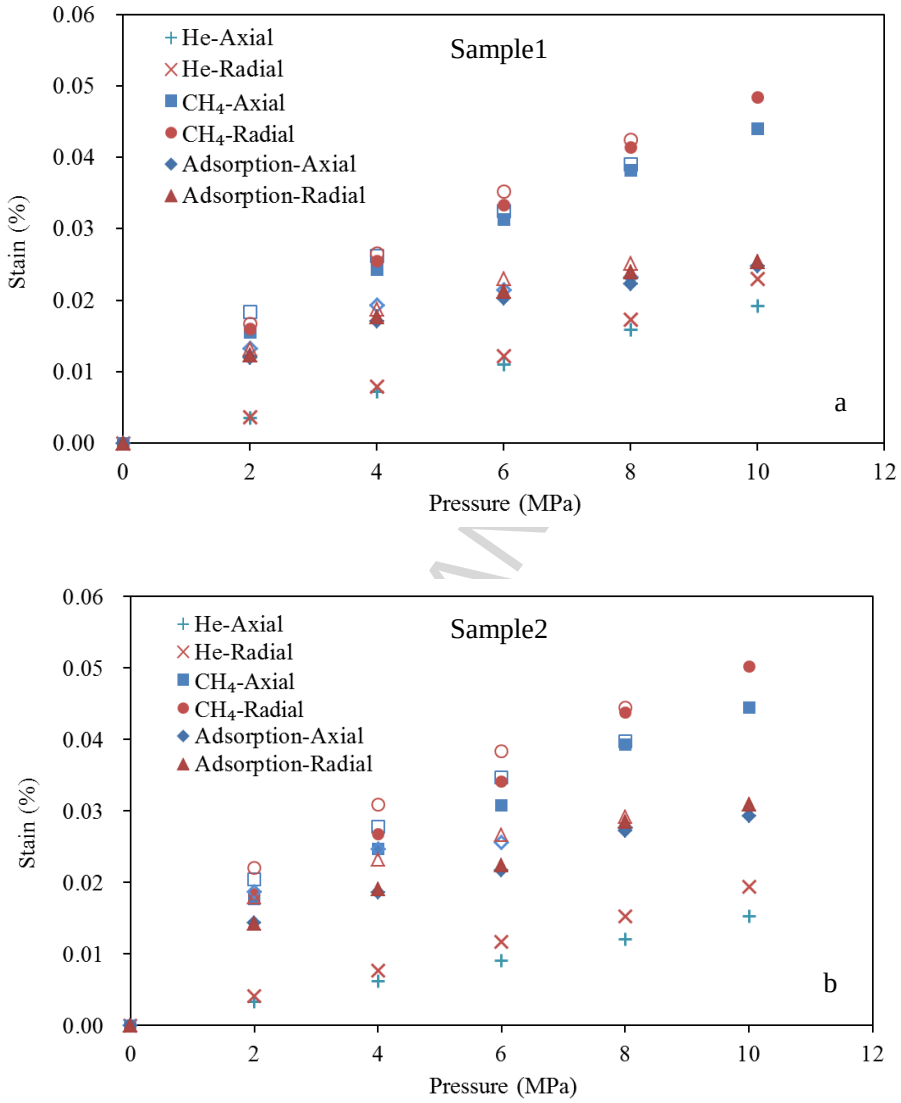

Fig. 13. Anisotropic strain behaviour (solid symbol: pressure increase cycle; empty symbol: pressure decrease cycle)

Highlights

Gas adsorption induced shale swelling is measured

The swelling strain is in the magnitude of 0.1% at methane pressure of 10 MPa for the shale studied

The swelling strain shows a Langmuir-like curve with respect to gas pressure

The swelling strain shows a linear relationship with methane adsorption amount

The swelling strain has a slight anisotropy and shows slight hysteresis for the adsorption and desorption cycles